THE JOURNAL OF PHYSICAL CHEMISTRY C

Article

pubs.acs.org/JPCC

Induced Charge Density and Thin Liquid Film at Hydrate/Methane Gas Interfaces

Felipe Jiménez-Ángeles[†] and Abbas Firoozabadi*[,†,‡]

[†]Reservoir Engineering Research Institute, Palo Alto, California 94301, United States

[‡]Department of Chemical and Environmental Engineering, Yale University, New Haven, Connecticut 06510, United States

Supporting Information

ABSTRACT: The hydrate/methane gas interface is studied by molecular dynamics simulations. Below the hydrate melting temperature a thin liquid film forms with an associated surface charge density and electrostatic potential. The thickness of the thin liquid film, the charge density, and electrostatic potential at the hydrate/gas interface are established at different subcooling temperatures for the first time. The hydrate interface has mixed polarity, being predominantly positive. A comparison is made with the ice/methane interface, which reveals similarities and differences in the induced charge density. The thin liquid film and the induced charge density have important implications for the interfacial properties of methane hydrates.

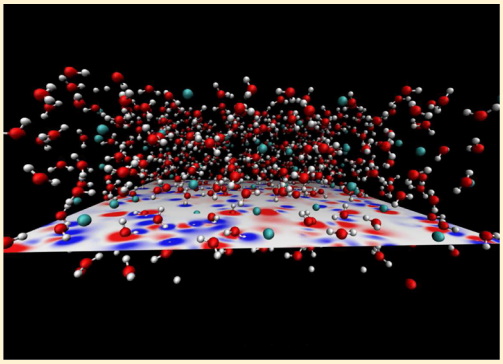

INTRODUCTION

Clathrate hydrates are icelike crystalline structures in which small molecules are encaged by hydrogen-bonded water.[1,2] Small hydrocarbon molecules, nitrogen, carbon dioxide, and hydrogen sulfide are some of the molecules that form hydrates. Structure I (sI) and structure II (sII) are the most common structures of clathrate hydrates. The structure and formation conditions (P, T) of clathrate hydrates are determined by the guest molecule.[3,4] The unit cell of sI is made up of 46 water molecules forming two dodecahedral cages (made of 20 water molecules located at 20 vertexes) and six tetradecahedral cages (24 water molecules); sI encages small gas molecules like methane and naturally occurs in deep oceans. The unit cell of sII consists of 136 water molecules forming 16 dodecahedral cages and eight hexadecahedral cages. Structure II is composed of molecules larger than ethane but smaller than pentane and forms frequently during hydrocarbon production and processing.[5]

During hydrocarbon production and transportation, formation of clathrate hydrates is a serious concern. Hydrates may obstruct pipelines and cause serious safety and environmental problems as well as economic losses.[3,6] Hydrates were formed in the 2010 oil spill in the Gulf of Mexico and caused failure of oil capture attempts.[7] Three-phase systems of oil, water, and gas are often encountered in hydrocarbon production. Small hydrate particles may form within water droplets in the oil phase and/or within the gas bubbles in the aqueous phase. The small hydrate particles can quickly agglomerate into larger hydrate solids.

There is vast interest in hydrates in the fields of energy, geology, planetary, and marine sciences; separation and sequestration processes; fuel transportation; climate change; and hydrogen storage.[8−14] Large reserves of methane hydrate exist under the sediments of the ocean floor and may become an important source of hydrocarbon energy.[15−17]

Similar to ice and other solids,[18−22] a thin liquid film on the surface of hydrates below their melting temperature may exist over a wide range of conditions (P, T) and interfaces, namely, hydrate/gas, hydrate/liquid-hydrocarbon, and hydrate/hydrate. Adhesion forces between hydrate surfaces, adsorption of different molecules on the hydrate surface (ions, oil components, surfactant molecules, polymers, etc.), viscosity of hydrate suspension, and interfacial tension, among other properties, are related to the interfacial behavior of hydrates.[23−33] The affinity of clathrate hydrates for ionic species[34,35] has been reported recently. In ice, large surface electrostatic potentials are well-established,[36] and it is known that ions can be adsorbed on the crystal surface conferring an effective charge.[37] The ice/water interface has been studied by molecular simulations.[38−40] To the best of our knowledge, a thin liquid film of clathrate hydrates has not been measured.

Molecular modeling of clathrate hydrate surfaces has focused mainly on describing heterogeneous hydrate nucleation and growth;[41−46] the modeling of the interfaces has been rarely investigated. Rodger et al. have observed the formation of a stable liquid film at the methane-hydrate/methane-gas interface.[47] In a similar study, Ding et al. have investigated the liquid layer formed during the melting of the hydrate crystal.[48] For ice, the thickness of the thin liquid layer has been studied by means of molecular dynamics simulations.[49,50]

Received: July 17, 2014
Revised: October 15, 2014
Published: October 20, 2014

   dx.doi.org/10.1021/jp507160s | J. Phys. Chem. C 2014, 118, 26041−26048

In this work, we examine the methane-hydrate/methane-gas interface by molecular dynamics simulations at temperatures below the melting point at a pressure of 100 bar. The number density, charge, and electrostatic potential profiles are studied as a function of subcooling for the first time.

MODELS AND SIMULATION METHOD

A two-phase system made of methane hydrates surrounded by methane gas phase is investigated. The setup is constructed as follows: A crystalline methane hydrate crystal made of 3 × 3 × 5 unit cells is created using the experimental parameters of sI.[51] The positions of hydrogen atoms are assigned based on the Bernal−Fowler rules.[52] The crystal consists of 2070 water molecules and 360 methane molecules placed in a box of dimensions $l_x \approx 3.5$ nm, $l_y \approx 3.5$ nm, and $l_z \approx 6$ nm in the x, y, and z directions, respectively. The structure is equilibrated during 0.5 ns by means of molecular dynamics simulations at T = 200 K and P = 100 bar under fully periodic boundary conditions. The crystal is then centered within a prismatic box of dimensions $l_x \approx 3.5$ nm, $l_y \approx 3.5$ nm, and $l_z \approx 14$ nm. 300 methane molecules are added at the empty spaces in the two sides of the slab. A first *NVT* molecular dynamics (MD) simulation is carried out at 200 K for 0.5 ps. The system is then pressurized to P = 100 bar and warmed for 3 ns at the following temperatures: 270, 280, 283, 285, 286, and 288 K. The resulting densities of methane in the gas phase range from 0.09 g/cm^3 at T = 270 K to 0.08 g/cm^3 at T = 288 K, which are consistent with a methane gas phase in bulk at the respective temperatures. The configurations are subjected to *NPT* simulations until the potential energy of the systems reaches a stationary state, which is defined as variations of less than 0.1 kJ/mol of the average potential energy for more than 10 ns. The melting temperature T_m is established at 287 ± 1 K as we will discuss below (the experimental melting temperature at 100 bar is 285.98 K[53]). Typical time to reach equilibration is more than 100 ns and can be up to 200 ns in some cases. For the melting temperature run, the simulation time is more than 400 ns. A subsequent *NVT* MD simulation is performed after equilibration for 30 ns to compute the number and charge densities and mean electrostatic potential profiles.

For comparison, we simulate the ice/methane interface consisting of an ice crystal of structure Ih next to a methane gas phase. The ice crystal is created using the experimental parameters of ice Ih,[54] and the hydrogen positions are assigned by means of the Bernal−Fowler rules.[52] The basal plane of ice is in contact with methane gas. The crystal slab has 2048 water molecules, and the gas phase is made of 512 methane molecules (half on each side). Initially, the dimensions of the crystal slab are $l_x \approx 3.6$ nm, $l_y \approx 2.7$ nm, and $l_z \approx 6.73$ nm in the x, y, and z directions, respectively. The crystal is equilibrated, centered in a prismatic box, and brought into contact with methane gas in a way similar to that used for the hydrate crystal. The box dimensions of the ice slab in equilibrium with methane are $l_x \approx 3.65$ nm, $l_y \approx 2.9$ nm, and $l_z \approx 20$ nm. At P = 100 bar, the melting temperature is established to be T = 270 K. The system is simulated at T = 269 K and P = 100 bar until the equilibrium is reached.

Water molecules are modeled by the TIP4P-ice[55] model while methane molecules are described as spherical particles. The methane molecule is modeled as a single particle which interacts with other particles thorough the Lennard-Jones potential. This model neglects electrostatic interactions and is computationally less expensive than the full atomistic models.[42] The parameters for methane are σ = 3.73 Å and ϵ = 1.23 kJ/mol. These values are obtained by fitting the pressure predicted by perturbation theory to the experimental values in the liquid−vapor coexistence region of methane.[56,57] The Lorentz−Berthelot combining rules are used for water−methane interactions. The simulations are performed using the open source code Gromacs.[58−60] Full periodic boundary conditions are applied in all directions. A time-step of 2 fs is used, which has been shown to be a reasonable choice in MD simulations of ice.[61] Short-range interactions are truncated at 1.2 nm, and long-range electrostatic interactions are computed using the smooth particle mesh Ewald summation of order 4 with a Fourier grid spacing of 0.16 nm and a tolerance of 10^{-5}. Berendsen thermostat and barostat smoothly drive the system toward a stabilized state even if the initial state is far from equilibrium. The Berendsen thermostat, however, does not produce velocity distribution consistent with the Boltzmann distribution. The Nosé−Hoover thermostat and Parrinello−Rahman barostat are less reliable toward equilibrium but are more suitable once the system is stabilized.[62] We use the Berendsen[63] thermostat and barostat to stabilize pressure and temperature during the 3 ns MD simulations with the parameters τ_T = 0.2 ps and τ_P = 0.5 ps. For the long simulation we use the Nosé−Hoover thermostat[64,65] with a relaxation time of τ_T = 2 ps and the Parrinello−Rahman[66] barostat with a relaxation time of τ_P = 10 ps. In independent simulations we used τ_P = 5 and 20 ps, and the results are similar to those for τ_p = 10 ps. The leapfrog algorithm is used for integrating Newton's equation of motion, and rigid water molecule constraints are implemented with the SHAKE algorithm.

The number density profiles are obtained from $\rho_i(z) = N_i(z)/(l_x l_y \Delta h_z)$, where $N_i(z)$ is the number of particles (i = O, H, and C for oxygen and hydrogen atoms and methane molecules, respectively) within a slice of thickness Δh_z = 0.2 Å along the z-direction. The charge density is given by $\rho_{el}(z) = q_O\rho_O(z) + q_H\rho_H(z)$, where $q_O = -1.1794$e and q_H = 0.5897e are, respectively, the charge of oxygen and hydrogen atoms of water molecule in the TIP4P-ice model. The charge of an oxygen atom is shifted from its center by δ_O = 0.1577 Å on the bisector of the angle formed by the two O−H bonds. The electric field along the z-direction,

$$E_z(z) = -\frac{d\psi(z)}{dz} \tag{1}$$

and the mean electrostatic potential profile, $\psi(z)$, are obtained by integrating Poisson's equation

$$\frac{d^2\psi(z)}{dz^2} = -\frac{1}{\epsilon_0}\rho_{el}(z) \tag{2}$$

The electric field along z is computed by

$$E_z(z) = \frac{1}{\epsilon_0}\int_{\infty}^{z} \rho_{el}(z)dz \tag{3}$$

and the mean electrostatic potential is obtained from

$$\psi(z) = -\int_{\infty}^{z} E_z(z)\, dz \tag{4}$$

with the boundary conditions

$$\psi(z \to \infty) = 0 \text{ and } E(z \to \infty) = 0 \tag{5}$$

where $z \to \infty$ is set at the box boundary in the z-direction. Alternatively, $E_z(z)$ can be computed by

dx.doi.org/10.1021/jp507160s | J. Phys. Chem. C 2014, 118, 26041−26048

$$E_z(z) = \frac{1}{4\pi\epsilon_0}\left\langle \sum_{\mathbf{n}}\sum_{i=1}^{3N_w} \frac{q_i(z - z_i - n_z l_z)}{|\mathbf{r} - \mathbf{r}_i - \mathbf{n}L|^3}\right\rangle \quad (6)$$

where q_i is the point charge located at $\mathbf{r}_i$ and $\mathbf{n}L$ is a translation vector to take into account the periodic images of the simulation box. z, z_i, and $n_z l_z$ are the z-components of vectors $\mathbf{r}$, $\mathbf{r}_i$, and $\mathbf{n}L$, respectively. The inner summation runs over the $3N_w$ point charges of water molecules while the outer one runs over the images of the box. Similarly, the mean electrostatic potential is given by

$$\psi(z) = \frac{1}{4\pi\epsilon_0}\left\langle \sum_{\mathbf{n}}\sum_{i=1}^{3N_w} \frac{q_i}{|\mathbf{r} - \mathbf{r}_i - \mathbf{n}L|}\right\rangle \quad (7)$$

The electric field and potential at z are computed on a grid of $n_g = 8 \times 8$ nodes with equidistant separation of $\Delta h_x \approx \Delta h_y \approx 0.45$ nm in the x and y directions. The electrostatic potential is computed with respect to the box boundary in the z-direction, whereas for the electric field in eq 6 there is no need to impose a boundary condition. The averages are computed from $N_c = 10^4$ independent configurations.

We define the local charge density per unit area as

$$\Sigma_{el}(z) = \rho_{el}(z)\Delta h_z \quad (8)$$

and the cumulative charge per unit area as

$$\sigma_{el}(z) = \int_{\infty}^{z} \rho_{el}(z)\, dz = \epsilon_0 E_z(z) \quad (9)$$

The local charge density $\Sigma_{el}(z)$ quantifies the charge average provided by the hydrogen and oxygen atoms within a slice between z and $z + \Delta h_z$. The cumulative charge density $\sigma_{el}(z)$ comprehends the charge from the box boundary to z; it is proportional to the electric field at z.

RESULTS

Figure 1 portrays the potential energy versus simulation time of the hydrate/methane gas setup at three different temperatures.

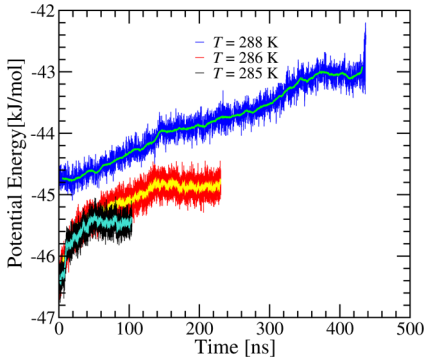

Figure 1. Potential energy as a function of time of the methane hydrate/methane gas setup at T = 285 K (black line), 286 K (red line), and 288 K (blue line); P = 100 bar in all cases. Light blue, yellow, and light green lines are averages calculated at intervals of 2 ns of the potential energy at T = 285, 286, and 288 K, respectively.

The profiles for the T = 285 and 286 K show an increasing trend and at some time reach a plateau; the average potential energies do not have variations of more than 0.1 kJ/mol. For T = 285 K, the plateau starts at around t = 50 ns and it is followed for more than 50 ns. For T = 286 K, the plateau starts from t = 140 ns and it is followed for more than 100 ns. The potential energy for T = 288 K increases for more than 360 ns and remains stationary for about 40 ns; then, the crystal becomes unstable and melts. The melting is signaled by a sudden increase of the potential energy. On the basis of these results we estimate the melting temperature at 287 ± 1 K. At the lower temperatures, the system reaches the plateau faster.

Snapshots of the configurations at the end of the long simulation run for subcoolings of $T_m - T$ = 17, 7, and 1 K are shown in panels a, b, and c of Figure 2, respectively. As

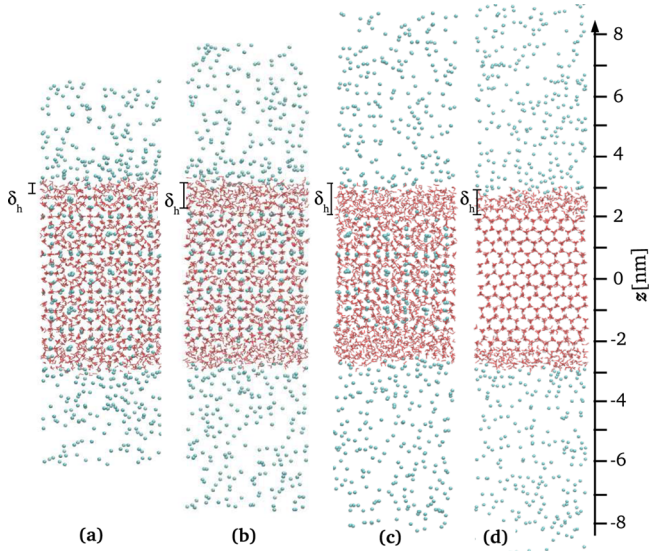

Figure 2. Snapshots of the hydrate/methane gas setups at (a) $T_m - T$ = 17 K, (b) $T_m - T$ = 7 K, and (c) $T_m - T$ = 1 K and (d) ice/methane interface at $T_m - T$ = 1 K. The pressure is P = 100 bar. At this pressure the computed melting temperatures are T_m = 287 K for the methane hydrate and T_m = 270 K for ice. Oxygen and hydrogen atoms of water are in red and white, respectively, and methane molecules are shown in green.

mentioned above, at P = 100 bar, the melting temperature is T_m = 287 ± 1 K. In the course of simulations the crystals dissociate at the interface and form a thin liquid layer. Nearly all the methane molecules from the melted cavities go toward the methane phase. Only one or two methane molecules remain in the liquid layer. The thickness of the liquid layer increases with increasing temperature (decreasing subcooling). For $T_m - T$ = 17 K, a few water molecules separate from the outermost layer of the crystal and produce a low-density disordered layer of about one water molecule thickness. At $T_m - T$ = 7 K, the water molecules of the two outermost crystal layers form a wider disordered region. For $T_m - T$ = 1 K, the thickness of the disordered region is around 1.4 nm. Figure 2d is a snapshot of the ice/methane interface at $T_m - T$ = 1 K. Similar to hydrates, a couple of molecules are dissolved in the liquid layer of ice. The thickness of the liquid layer is around 1 nm, which is close to the experimental value[18] and in agreement with some recent computer simulations.[49]

The density profiles of oxygen, hydrogen, and methane molecules along the z-direction of the hydrate/methane gas setup are shown in Figure 3a for $T_m - T$ = 1 K. Periodic sharp peaks in the hydrate region are observed. The methane density profile has two repeating peaks, one higher than the other, whereas oxygen profiles exhibit a twin peak separated from the third. The hydrogen profile has a high peak with two shoulders separated from a single peak. The periodicity is about 6 Å and is

dx.doi.org/10.1021/jp507160s | J. Phys. Chem. C 2014, 118, 26041−26048

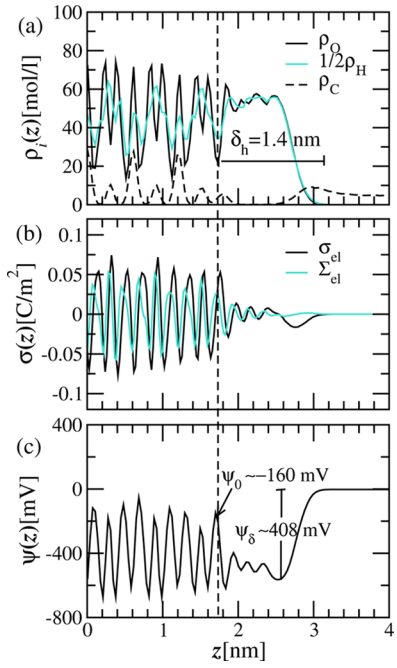

Figure 3. Hydrate/methane gas interface at 1 K subcooling and P = 100 bar. (a) Number density profiles of oxygen (solid black line) and methane (dashed line) and half of the density profile of hydrogen (solid light-blue line). (b) Local charge density (light blue line) and integrated charge density (black line) profiles. (c) Mean electrostatic potential profile. Simulation temperature is T = 286 K, and the melting temperature is T_m = 287 ± 1 K. The hydrate crystal is centered at z = 0. For clarity only the interval for z > 0 is shown. The vertical dashed line is the hydrate-liquid layer boundary.

related to methane hydrate structure and orientation. Next to the crystal, the periodicity breaks and the density profiles have an interval with no well-defined peaks. The density profile of oxygen fluctuates around 55 mol/L from $z \approx 2-2.6$ nm and goes to zero at $z \approx 3.1$ nm. The disordered region is the thin liquid layer. The hydrate-liquid layer boundary can be defined at the minimum of the oxygen density profile where the disordered phase starts (see Figure 3).

The last methane peak is at $z \approx 1.8$ nm. Beyond this peaks there is a region depleted from methane for approximately 8 Å. The methane density increases in the interval where the oxygen profile decreases. In this interval water and methane are mixed. The methane density profile reaches a maximum close to the point where the profiles of oxygen and hydrogen go to zero and becomes constant in the methane gas phase. A similar enhancement of methane local density near the liquid layer has been observed in water/methane interfaces.[67] The structure of the disordered layer exhibits similarities to the hydrate structure as subcooling increases (see Supporting Information), whereas it becomes structureless at temperatures close to the melting point.

Figure 3b shows the density of charge per unit area $\Sigma_{el}(z)$ and the cumulative charge per unit area $\sigma_{el}(z)$ along the z-direction of the hydrate/methane gas setup at 1 K subcooling. The former is the local charge, whereas the latter is proportional to the electric field (see eqs 8 and 9). Both functions show a periodic behavior with maximum and minimum close to ±0.05 C/m^2 in the hydrate region. The two functions are slightly shifted with respect to each other. Interestingly, at the boundary between the crystal and the liquid layer, the electric field and charge are positive. This is related to the outnumbering of hydrogen atoms over oxygen atoms at the hydrate-liquid layer boundary seen in the number density profiles (Figure 3a). The values of the surface charge density and cumulative surface charge density are close to 0.05 C/m^2. In the liquid region both functions display a damped oscillatory behavior. Close to the liquid-methane interface there is still a charge imbalance which produces a negative electric field. Outside the liquid region toward the gas phase the surface charge profiles go to zero. Electroneutrality is only locally broken. As a whole, the crystal-liquid interface is neutral.

The mean electrostatic potential profile $\psi(z)$ is depicted in Figure 3c. The charge imbalance at the thin liquid film/methane gas interface produces a significant potential drop. In the liquid layer the potential oscillates, and close to the hydrate/liquid layer boundary it reaches a value of −160 mV. The electrostatic potential difference between the hydrate/liquid layer boundary and the minimum close to the methane gas phase ψ_δ is about 408 mV. The negative slope of the potential profile at the hydrate/liquid layer boundary is important because it implies a positive value of the electric field at this point, as discussed above. The density profiles and cumulative charge densities for lower subcoolings are shown in the Supporting Information.

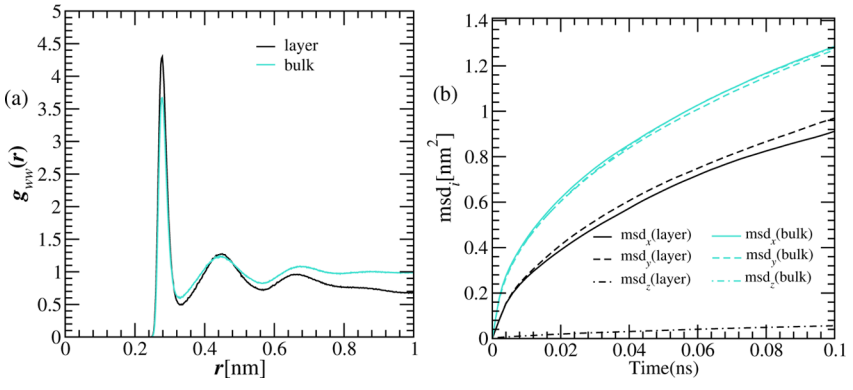

Figure 4. Structural and dynamical properties of the disordered layer. (a) Water−water radial distribution function profiles in the liquid layer (black line) and in the bulk (light blue line). (b) Components of the mean square displacement as a function of time in the liquid layer (black lines) and in the bulk (light blue lines); x and z components of the MSD in bulk are overlapped, whereas the y component is slightly lower. T = 286 K and P = 100 bar equivalent to 1 K subcooling for the hydrate.

dx.doi.org/10.1021/jp507160s | J. Phys. Chem. C 2014, 118, 26041−26048

To verify that the interfacial disordered layer at the methane/hydrate interface is a liquid, we examine the structural and dynamical properties. The structural properties are investigated by means of the radial distribution function (RDF) profiles, whereas the dynamical properties are studied by means of the mean square displacement as a function of time. The RDF profile gives the probability density of finding a second particle at a distance r from a central particle. Figure 4a shows the RDF profile of water molecules in the liquid layer and in the bulk. Both profiles are similar in the location of their peaks but with different heights. Because of the low ordering shown in the RDF profile, it is clear that the water in the disordered interface is a liquid. The tilted arrangement of the liquid-layer RDF profile is related to the confinement of water molecules in the z direction.

The mean square displacement (MSD) $d(t)$ is related to the self-diffusion coefficient D_s by $d^2(t) = D_s t$. The MSD is calculated from $d^2(t) = \langle(\mathbf{r}(t + t') - \mathbf{r}(t')) \cdot (\mathbf{r}(t + t') - \mathbf{r}(t'))\rangle$, where $\mathbf{r}(t')$ and $\mathbf{r}(t' + t)$ are the positions of a particle at t' and $t + t'$, respectively. The averages are computed over a set of particles and a set of time intervals with a lag time of t'. In terms of the x, y, and z components, the mean square displacement is expressed as $d^2(t) = \langle(x(t + t') - x(t'))^2\rangle + \langle(y(t + t') - y(t'))^2\rangle + \langle(z(t + t') - z(t'))^2\rangle$. Figure 4b shows the components of the mean square displacement of water molecules in the liquid layer and in the bulk. As expected, the components of the bulk MSD are similar. The x and y components of the MSD of the interfacial hydrate liquid layer are similar, whereas the z component is much less. The lower value of the layer MSD components with respect to the bulk values is related to the quasi two-dimensional arrangement of water molecules in the liquid layer, which is magnified in the z direction.

To validate our approach for computing the mean electrostatic field through integration of the density profiles, namely eq 3, we compare it with the result obtained from direct summation of Coulomb terms given in eq 6. A similar comparison is carried out for the mean electrostatic potential obtained from eqs 4 and 7. Figure 5a shows the mean electric field profiles from the two different methods while Figure 5b shows the mean electrostatic potential profiles. There are some statistical fluctuations for the electric field in the liquid layer computed from direct summation of Coulomb terms. The agreement between the two methods is good for the mean electrostatic potential and the electric field.

We also investigate density, surface charge density, and electric potential of ice at $T_m - T = 1$ K and $P = 100$ bar ($T_m = 270$ K). Figure 6a shows the density profiles of oxygen and methane and the profile of half density of hydrogen of the ice/methane gas setup. The periodic structure of ice is in the interval $z < 2.4$ nm and the liquid layer from $z \approx 2.38$ to 3.4 nm. In the liquid layer there is some structure reminiscent of ice with two overlapped peaks and a minimum between the peaks. The peak closer to the crystal has a shoulder resembling the twin peak structure from the crystal. The density at the highest peak in the liquid layer is ~80 mol/L and at the shoulder is close to the density of bulk water ~55 mol/L.

The density of charge per unit area $\Sigma_{el}(z)$ and the cumulative charge per unit area $\sigma_{el}(z)$ along the z axis of the ice/methane gas setup are shown in Figure 6b. At the boundary between the crystal and the liquid layer, the electric field and charge are positive similar to those at the hydrate/methane interface. At this boundary the surface charge density is higher than that for the hydrate at the equivalent location (>0.05 C/m^2). In the liquid layer the cumulative charge and charge density profiles oscillate and go to zero at the methane gas region. The mean electrostatic potential profile $\psi(z)$ is shown in Figure 6c. At the crystal/liquid layer boundary the mean electrostatic potential is ~26 mV and decreases to a minimum value ~ −720 mV. The electrostatic potential difference between the ice-liquid layer boundary and the minimum close to gas phase ψ_δ is about 690 mV.

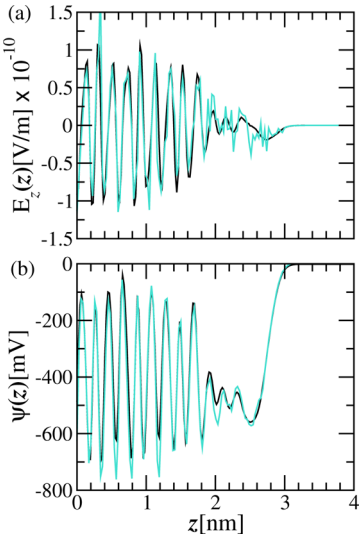

Figure 5. (a) Mean electric field obtained from eq 3 (black line) and from eq 6 (light blue line). (b) Mean electrostatic potential from eq 4 (black line) and eq 7 (light blue line). $T = 286$ K and $P = 100$ bar equivalent to 1 K subcooling for the hydrate.

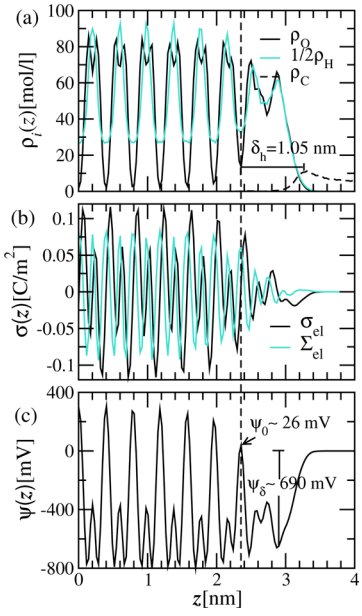

Figure 6. Ice/methane interface at 1 K subcooling and $P = 100$ bar. (a) Density profiles of oxygen (solid black line) and methane (dashed line) and half of the density profile of hydrogen (light blue line). (b) Local surface charge density (light blue line) and integrated surface charge density (black line) profiles. (c) Mean electrostatic potential profile. The melting temperature is $T_m = 270$ K. The hydrate crystal is centered at $z = 0$. For clarity only the interval for $z > 0$ is shown. The vertical dashed line is the ice-liquid layer boundary.

dx.doi.org/10.1021/jp507160s | J. Phys. Chem. C 2014, 118, 26041−26048

The thickness of the liquid layer δ_h in the hydrate is shown in Figure 7 as a function of subcooling $(T_m - T)$. At the simulated

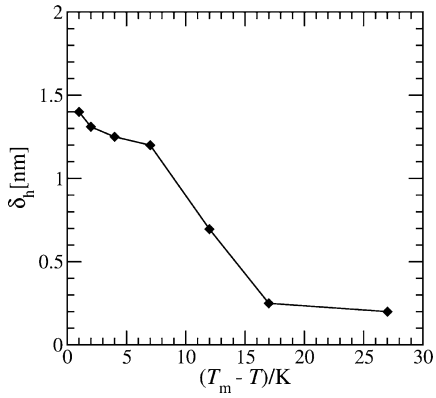

Figure 7. Liquid layer thickness δ_h at the methane hydrate/methane gas interface as a function of subcooling.

subcooling of 1 K, the liquid layer thickness is 1.4 nm and decreases as subcooling increases. Only for the subcooling range $\lesssim$11 K is the layer thickness larger than 6 Å, which corresponds to approximately two water molecules. For the two highest subcooling conditions the thin liquid is around 2 Å implying that only the water molecules at the outermost layer are disordered. For ice, measured data shows that as we approach the melting point the liquid film thickness increases sharply.[18] This may be also the same for hydrates. The results presented in Figure 7 do not show the sharp increase in film thickness as melting point is approached. The difference between data and theory may be related to the water potential model and size of the system. A similar behavior is observed in molecular simulations of ice.[50]

The surface charge density Σ_{el}^0 and the cumulative surface charge density σ_{el}^0 at the hydrate/liquid layer boundary are shown in Figure 8a as a function of subcooling. The highest value of the surface charge density at the boundary is for 1 K of subcooling. For the higher subcoolings the value is 0.035 to 0.04 C/m^2. The cumulative surface charge density has values between 0.028 and 0.042 C/m^2 for the range of subcooling temperatures between 1 and 11 K. The mean electrostatic potential at the boundary between the hydrate and the liquid layer ψ_0 is around −200 mV (Figure 8b). The mean electrostatic potential difference between the hydrate-liquid layer boundary and the liquid layer ψ_δ oscillates around 400 mV in the range of subcooling between 1 and 11 K.

The positive charge density at the methane hydrate/thin liquid layer interface is because of the outnumbering of protons over oxygen atoms. To have a full picture of the interface, we make use of the three-dimensional (3D) charge density profiles defined as $\rho_{el}(x, y, z) = q_O\rho_O(x, y, z) + q_H\rho_H(x, y, z)$ where the 3D number density profiles are given by $\rho_i(x, y, z) = N_i(x, y, z)/(\Delta h_x \Delta h_y \Delta h_z)$, where $N_i(x, y, z)$ is the number of particles (i = O, H) within a rectangular prism of volume $\Delta h_x \Delta h_y \Delta h_z$ at x, y, and z. A two-dimensional (2D) surface charge density at a given $z = z_0$ can be defined as $\Sigma_{el}(x,y) = \rho_{el}(x,y,z_0)\Delta h_z$. The 1D and 2D surface charge densities are related by $\Sigma_{el}(z_0)l_x l_y = \int_0^{l_x}\int_0^{l_y}\Sigma_{el}(x,y)\,dx\,dy$. For our calculation, we use $\Delta h_x = \Delta h_y \approx$ 0.1 Å and Δh_z = 0.2 Å. In Figure 9, $\Sigma_{el}(x,y)$ at $z_0 \approx$ 1.7 nm is

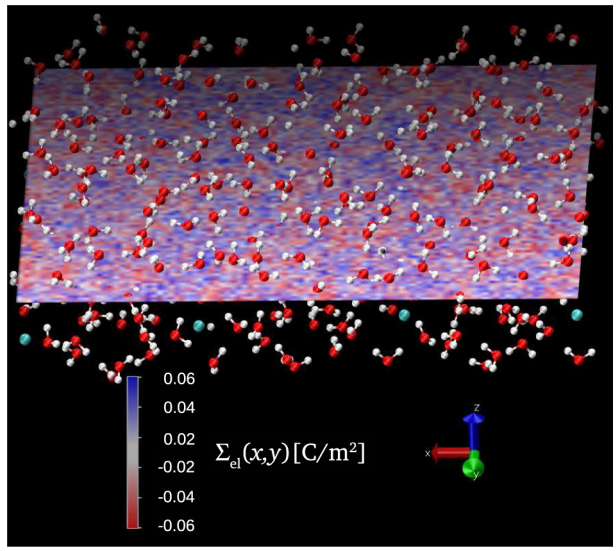

Figure 9. Snapshot of an instantaneous configuration of a layer of water molecules at the methane-hydrate/thin liquid film interface at $T_m - T$ = 1 K. In the background is the averaged charge density profile Σ_{el} as a function of (x, y) at $z_0 \approx$ 1.7 nm. Blue zones indicate positive charge, whereas red indicates negative charge. Oxygen and hydrogen atoms of water are in red and white, respectively, and methane molecules are shown in green.

shown in a 2D plot. The positive values of the surface charge density are shown in blue tones, whereas the negative values are

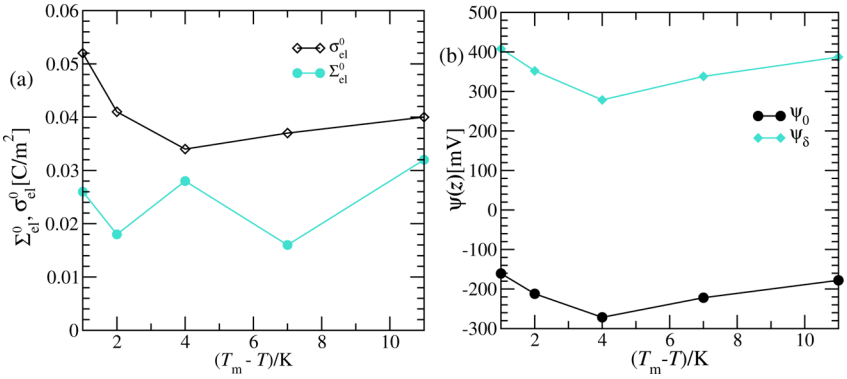

Figure 8. (a) Charge density σ_{el}^0 and cumulative charge density Σ_{el}^0 at the hydrate-liquid layer boundary as a function of subcooling. (b) Mean electrostatic potential at the hydrate-liquid layer boundary ψ_0 and electroatatic potential difference ψ_δ between the hydrate/liquid layer boundary and the minimum close to methane gas phase.

dx.doi.org/10.1021/jp507160s | J. Phys. Chem. C 2014, 118, 26041−26048

in red. The average charge density at some regions on the $x-y$ plane is as high (low) as 0.2 C/m^2 (−0.2 C/m^2). The surface charge density at the interface ($z_0 \approx 1.7$ nm) is $\Sigma_{el} \approx 0.05$ C/m^2. An instantaneous configuration of water molecules at the methane hydrate/liquid layer interface ($x-y$ plane) is shown in Figure 9.

CONCLUSIONS

The thin liquid film at the hydrate/methane gas interface is studied by molecular dynamics simulations. We have established the thickness of the hydrate liquid layer, surface charge density, and interfacial potential as a function of subcooling at P = 100 bar. At 1 K subcooling the thickness is 1.4 nm. The outnumbering of protons over oxygen atoms produces a positive surface charge density. The surface charge density at the hydrate-liquid interface is around 0.05 C/m^2, and the mean electrostatic potential is −160 mV at 1 K subcooling. The local fluctuations of the surface charge can be as large as ±0.2 C/m^2. These high values imply that electrostatic effects at the methane hydrate/methane gas interface may make important contributions to the interfacial properties.

ASSOCIATED CONTENT

Supporting Information

Density profiles and cumulative charge densities for lower subcoolings (T = 275, 280, 283, and 285 K; Figures S1−S4). This material is available free of charge via the Internet at http://pubs.acs.org

AUTHOR INFORMATION

Corresponding Author

*E-mail: abbas.firoozabadi@yale.edu. Phone: +1 (650)326-9172. Fax: +1 (650) 472-9285.

Notes

The authors declare no competing financial interest.

ACKNOWLEDGMENTS

We thank the member companies of the Reservoir Engineering Research Institute (RERI) for their financial support.

REFERENCES

(1) Englezos, P. Clathrate Hydrates. *Ind. Eng. Chem. Res.* **1993**, *32*, 1251−1274.
(2) Koh, C. A. Towards a Fundamental Understanding of Natural Gas Hydrates. *Chem. Soc. Rev.* **2002**, *31*, 157−167.
(3) Sloan, E. D.; Koh, C. A. *Clathrate Hydrates of Natural Gases*; CRC Press: Boca Raton, FL, 2008.
(4) Buffett, B. A. Clathrate Hydrates. *Annu. Rev. Earth Planet. Sci.* **2000**, *28*, 477−507.
(5) Sloan, E. D. Gas Hydrates: Review of Physical/Chemical Properties. *Energy Fuels* **1998**, *12*, 191−196.
(6) Bagirov, E.; Lerche, I. Hydrates Represent Gas Source, Drilling Hazard. *Oil Gas J.* **1997**, *95*, 99−104.
(7) Graham, B.; Reilli, W. K.; Beinecke, F.; Boesch, D. F.; Garcia, T. D.; Murray, C. A.; Ulmer, F. Deep Water: The Gulf Oil Disaster and the Future of Offshore Drilling - Report to the President (BP Oil Spill Commission Report). 2011.
(8) Park, Y.; Kim, D.-Y.; Lee, J.-W.; Huh, D.-G.; Park, K.-P.; Lee, J.; Lee, H. Sequestering Carbon Dioxide into Complex Structures of Naturally Occurring Gas Hydrates. *Proc. Natl. Acad. Sci. U.S.A.* **2006**, *103*, 12690−12694.
(9) Chatti, I.; Delahaye, A.; Fournaison, L.; Petitet, J.-P. Benefits and Drawbacks of Clathrate Hydrates: A Review of Their Areas of Interest. *Energy Convers. Manage.* **2005**, *46*, 1333−1343.
(10) Glasby, G. P. Potential Impact on Climate of the Exploitation of Methane Hydrate Deposits Offshore. *Mar. Pet. Geol.* **2003**, *20*, 163−175.
(11) Florusse, L. J.; Peters, C. J.; Schoonman, J.; Hester, K. C.; Koh, C. A.; Dec, S. F.; Marsh, K. N.; Sloan, E. D. Stable Low-Pressure Hydrogen Clusters Stored in a Binary Clathrate Hydrate. *Science* **2004**, *306*, 469−471.
(12) Mao, W. L.; Mao, H.-K.; Goncharov, A. F.; Struzhkin, V. V.; Guo, Q.; Hu, J.; Shu, J.; Hemley, R. J.; Somayazulu, M.; Zhao, Y. Hydrogen Clusters in Clathrate Hydrate. *Science* **2002**, *297*, 2247−2249.
(13) Reagan, M. T.; Moridis, G. J. Global Climate and the Response of Oceanic Hydrate Accumulations. *Fire in the Ice: Methane Hydrate Newsletter* **2010**, *10*, 9−12.
(14) Koh, C. A.; Sloan, E. D.; Sum, A. K.; Wu, D. T. Fundamentals and Applications of Gas Hydrates. *Annu. Rev. Chem. Bio. Eng.* **2011**, *27*, 237−257.
(15) Collett, T. S.; Kuuskraa, V. A. Hydrates Contain Vast Store of World Gas Resources. *Oil Gas J.* **1998**, *96*, 90−95.
(16) Lee, S.-Y.; Holder, G. D. Methane Hydrates Potential as a Future Energy Source. *Fuel Process. Technol.* **2001**, *71*, 181−186.
(17) Sloan, E. D. Fundamental Principles and Applications of Natural Gas Hydrates. *Nature (London, U.K.)* **2003**, *426*, 353−363.
(18) Dash, J. G.; Rempel, A. W.; Wettlaufer, J. S. The Physics of Premelted Ice and its Geophysical Consequences. *Rev. Mod. Phys.* **2006**, *78*, 695−741.
(19) Häkkinen, H.; Manninen, M. Computer Simulation of Disordering and Premelting of Low-Index Faces of Copper. *Phys. Rev. B: Condens. Matter Mater. Phys.* **1992**, *46*, 1725−1742.
(20) Frenken, J. W. M.; Veen, J. F. v. d. Observation of Surface Melting. *Phys. Rev. Lett.* **1985**, *54*, 134−137.
(21) Stock, K.; Menzel, E. Probing the Surface Melt of Copper Crystals. *J. Cryst. Growth* **1980**, *43*, 135−138.
(22) Zhu, D.-M.; Pengra, D.; Dash, J. G. Edge Melting in Two-Dimensional Solid Films. *Phys. Rev. B: Condens. Matter Mater. Phys.* **1988**, *37*, 5586−5593.
(23) Taylor, C. J.; Dieker, L. E.; Miller, K. T.; Koh, C. A.; Sloan, E. D. Micromechanical Adhesion Force Measurements Between Tetrahydrofuran Hydrate Particles. *J. Colloid Interface Sci.* **2007**, *306*.
(24) Zerpa, L. E.; Salagerand, J.-L.; Koh, C. A.; Sloan, E. D.; Sum, A. K. Surface Chemistry and Gas Hydrates in Flow Assurance. *Ind. Eng. Chem. Res.* **2011**, *50*, 188−197.
(25) Maeda, N.; Aman, Z. M.; Kozielski, K. A.; Koh, C. A.; Sloan, E. D.; Sum, A. K. Measurements of Cohesion Hysteresis between Cyclopentane Hydrates in Liquid Cyclopentane. *Energy Fuels* **2013**, *27*, 5168−5174.
(26) Dieker, L. E.; Aman, Z. M.; George, N. C.; Sum, A. K.; Sloan, E. D.; Koh, C. A. Micromechanical Adhesion Force Measurements between Hydrate Particles in Hydrocarbon Oils and Their Modifications. *Energy Fuels* **2009**, *23*, 5966−5971.
(27) Song, J. H.; Couzis, A.; Lee, J. W. Investigation of Macroscopic Interfacial Dynamics between Clathrate Hydrates and Surfactant Solutions. *Langmuir* **2010**, *26*, 18119−18124.
(28) Webb, E. B.; Rensing, P. J.; Koh, C. A.; Sloan, E. D.; Sum, A. K.; Liberatore, M. W. High-Pressure Rheology of Hydrate Slurries Formed from Water-in-Oil Emulsions. *Energy Fuels* **2012**, *26*, 3504−3509.
(29) Webb, E. B.; Koh, C. A.; Liberatore, M. W. Rheological Properties of Methane Hydrate Slurries Formed from AOT + Water + Oil Microemulsions. *Langmuir* **2013**, *29*, 10997−11004.
(30) Aman, Z. M.; Olcott, K.; Pfeiffer, K.; Sloan, E. D.; Sum, A. K.; Koh, C. A. Surfactant Adsorption and Interfacial Tension Investigations on Cyclopentane Hydrate. *Langmuir* **2013**, *29*, 2676−2682.
(31) Aman, Z. M.; Dieker, L. E.; Aspenes, G.; Sum, A. K.; Sloan, E. D.; Koh, C. A. Influence of Model Oil with Surfactants and Amphiphilic Polymers on Cyclopentane Hydrate Adhesion Forces. *Energy Fuels* **2010**, *24*, 5441−5445.

(32) Song, J. H. K.; Couzis, A.; Lee, J. W. Direct Measurements of Contact Force between Clathrate Hydrates and Water. *Langmuir* **2010**, *26*, 9187−9190.
(33) Aman, Z. M.; Leith, W. J.; Grasso, G. A.; Sloan, E. D.; Sum, A. K.; Koh, C. A. Adhesion Force between Cyclopentane Hydrate and Mineral Surfaces. *Langmuir* **2013**, *29*, 15551−15557.
(34) Qi, Y.; Wu, W.; Liu, Y.; Xie, Y.; Chen, X. The Influence of NaCl Ions on Hydrate Structure and Thermodynamic Equilibrium Conditions of Gas Hydrates. *Fluid. Phase Equil.* **2012**, *325*, 6−10.
(35) Farhang, F.; Nguyen, A. V.; Hampton, M. A. Influence of Sodium Halides on the Kinetics of CO_2 Hydrate Formation. *Energy Fuels* **2014**, *28*, 1220−1229.
(36) Petrenko, V. *The Surface of Ice*; Special Report 94-22; US Army Corps of Engineers, Cold Regions Research and Engineering Laboratory, 1994.
(37) Čop, A.; Kallay, N. *Trends in Colloid and Interface Science XVII*; Progress in Colloid and Polymer Science; Springer: Berlin, 2004; Vol. *126*; p 83.
(38) Karim, O. A.; Haymet, A. D. J. The Ice/Water Interface: A Molecular Dynamics Simulation Study. *J. Chem. Phys.* **1988**, *89*, 6889−6896.
(39) Nada, H.; Furukawa, Y. Anisotropy in Structural Phase Transitions at Ice Surfaces: A Molecular Dynamics Study. *Appl. Surf. Sci.* **1997**, *121*, 445−447.
(40) Razul, M. S. G.; Kusalik, P. G. Crystal Growth Investigations of Ice/Water Interfaces from Molecular Dynamics Simulations: Profile Functions and Average Properties. *J. Chem. Phys.* **2011**, *134*, 014710.
(41) Vatamanu, J.; Kusalik, P. G. Molecular Insights into the Heterogeneous Crystal Growth of sI Methane Hydrate. *J. Phys. Chem. B* **2006**, *110*, 15896−15904.
(42) Tung, Y.-T.; Chen, L.-J.; Chen, Y.-P.; Lin, S.-T. The Growth of Structure I Methane Hydrate from Molecular Dynamics Simulations. *J. Phys. Chem. B* **2010**, *114*, 10804−10813.
(43) Vatamanu, J.; Kusalik, P. G. Observation of Two-Step Nucleation in Methane Hydrates. *Phys. Chem. Chem. Phys.* **2010**, *12*, 15065−15072.
(44) Jacobson, L. C.; Hujo, W.; Molinero, V. Amorphous Precursors in the Nucleation of Clathrate Hydrates. *J. Am. Chem. Soc.* **2010**, *132*, 11806−11811.
(45) Jacobson, L. C.; Molinero, V. Can Amorphous Nuclei Grow Crystalline Clathrates? The Size and Crystallinity of Critical Clathrate Nuclei. *J. Am. Chem. Soc.* **2011**, *133*, 6458−6463.
(46) English, N. J.; MacElroy, J. M. D. Perspectives on Molecular Simulation of Clathrate Hydrates: Progress, Prospects and Challenges. *Chem. Eng. Sci.* **2014**, In press.
(47) Rodger, P. M.; Forester, T. R.; Smith, W. Simulations of the Methane Hydrate/Methane Gas Interface Near Hydrate Forming Conditions. *Fluid Phase Equilib.* **1996**, *116*, 326−332.
(48) Ding, L.; Geng, C.; Zhao, Y.; He, X.; Wen, H. Molecular Dynamics Simulation for Surface Melting and Self-Preservation Effect of Methane Hydrate. *Sci. China Ser. B: Chem.* **2008**, *51*, 651−660.
(49) Shepherd, T. D.; Koc, M. A.; Molinero, V. The Quasi-Liquid Layer of Ice under Conditions of Methane Clathrate Formation. *J. Phys. Chem. C* **2012**, *116*, 12172−12180.
(50) Conde, M. M.; Vega, C.; Patrykiejew, A. The Thickness of a Lliquid Layer on the Free Surface of Ice as Obtained from Computer Simulation. *J. Chem. Phys.* **2008**, *129*, 014702.
(51) Kirchner, M. T.; Boese, R.; Billups, W. E.; Norman, L. R. Gas Hydrate Single-Crystal Structure Analyses. *J. Am. Chem. Soc.* **2004**, *126*, 9407−9412.
(52) Bernal, J. D.; Fowler, R. H. A Theory of Water and Ionic Solution, with Particular Reference to Hydrogen and Hydroxyl Ions. *J. Chem. Phys.* **1933**, *1*, 515−548.
(53) Roo, J. L. D.; Peters, C. J.; Lichtenthaler, R. N.; Diepen, G. A. M. Occurrence of Methane Hydrate in Saturated and Unsaturated Solutions of Sodium Chloride and Water in Dependence of Temperature and Pressure. *AIChE J.* **1983**, *29*, 651−657.
(54) Kuhs, W. F.; Lehmann, M. S. The Structure of Ice-Ih. *Water Sci. Rev.* **1986**, 1−66.
(55) Abascal, J. L. F.; Sanz, E.; García Fernández, R.; Vega, C. A Potential Model for the Study of Ices and Amorphous Water: TIP4P/Ice. *J. Chem. Phys.* **2005**, *122*, 234511−1−9.
(56) Jorgensen, W. L.; Madura, J. D.; Swenson, C. J. Optimized Intermolecular Potential Functions for Liquid Hydrocarbons. *J. Am. Chem. Soc.* **1984**, *106*, 6638−6646.
(57) Verlet, L.; Weis, J.-J. Perturbation Theory for the Thermodynamic Properties of Simple Liquids. *Mol. Phys.* **1972**, *24*, 1013−1024.
(58) Berendsen, H.; Spoel, D. V. D.; Drunen, R. V. GROMACS: A Message-Passing Parallel Molecular Dynamics Implementation. *Comput. Phys. Commun.* **1995**, *91*, 43−56.
(59) Spoel, D. V. D.; Lindahl, E.; Hess, B.; Groenhof, G.; Mark, A. E.; Berendsen, H. J. C. GROMACS: Fast, Flexible, and Free. *J. Comput. Chem.* **2005**, *26*, 1701−1718.
(60) Hess, B.; Kuttner, C.; van der Spoel, D.; Lindahl, E. GROMACS 4: Algorithms for Highly Efficient, Load-Balanced, and Scalable Molecular Simulation. *J. Chem. Theory Comput.* **2008**, *4*, 435−447.
(61) Rozmanov, D.; Kusalik, P. G. Anisotropy in the Crystal Growth of Hexagonal ice, Ih. *J. Chem. Phys.* **2012**, *137*, 094702.
(62) Berendsen, H. J. C. *Simulating the Physical World: Hierarchical Modeling from Quantum Mechanics to Fluid Dynamics*; Cambridge University Press: Cambridge, U.K., 2007.
(63) Berendsen, H. J. C.; Postma, J. P. M.; van Gunsteren, W. F.; Di Nola, A.; Haak, J. R. Molecular-Dynamics with Coupling to an External Bath. *J. Chem. Phys.* **1984**, *81*, 3684−3690.
(64) Nose, S. A Unified Formulation of the Constant Temperature Molecular-Dynamics Methods. *J. Chem. Phys.* **1984**, *81*, 511−519.
(65) Hoover, W. G. Canonical dynamics: Equilibrium Phase-Space Distributions. *Phys. Rev. A: At., Mol., Opt. Phys.* **1985**, *31*, 1695−1697.
(66) Parrinello, M.; Rahman, A. Crystal Structure and Pair Potentials: A Molecular-Dynamics Study. *Phys. Rev. Lett.* **1980**, *45*, 1196−1199.
(67) English, N. J.; Lauricella, M.; Meloni, S. Massively Parallel Molecular Dynamics Simulation of Formation of Clathrate-Hydrate Precursors at Planar Water-Methane Interfaces: Insights Into Heterogeneous Nucleation. *J. Chem. Phys.* **2014**, *140*.